frontiers in Energy Research

ORIGINAL RESEARCH
published: 10 September 2018
doi: 10.3389/fenrg.2018.00089

Effect of AlF_3-Coated $Li_4Ti_5O_{12}$ on the Performance and Function of the $LiNi_{0.5}Mn_{1.5}O_4$||$Li_4Ti_5O_{12}$ Full Battery—An *in-operando* Neutron Powder Diffraction Study

Gemeng Liang[1], Anoop Somanathan Pillai[1], Vanessa K. Peterson[1,2], Kuan-Yu Ko[3], Chia-Ming Chang[3], Cheng-Zhang Lu[3], Chia-Erh Liu[3], Shih-Chieh Liao[3], Jin-Ming Chen[3], Zaiping Guo[1] and Wei Kong Pang[1]**

[1] Faculty of Engineering, Institute for Superconducting & Electronic Materials, University of Wollongong, Wollongong, NSW, Australia, [2] Australian Centre for Neutron Scattering, Australian Nuclear Science and Technology Organization, Sydney, NSW, Australia, [3] Department of Nanomaterials for Energy Storage, Material & Chemical Research Laboratory, Industrial Technology Research Institute, Hsinchu, Taiwan

OPEN ACCESS

Edited by:
Verónica Palomares, University of the Basque Country, Spain

Reviewed by:
Stephen Hull, Science and Technology Facilities Council, United Kingdom
Jordi Jacas Biendicho, Institut de Recerca de l'Energia de Catalunya, Spain

***Correspondence:**
Vanessa K. Peterson
vanessa.peterson@ansto.gov.au
Wei Kong Pang
wkpang@uow.edu.au

Specialty section:
This article was submitted to Energy Storage, a section of the journal Frontiers in Energy Research

Received: 01 April 2018
Accepted: 17 August 2018
Published: 10 September 2018

Citation:
Liang G, Pillai AS, Peterson VK, Ko K-Y, Chang C-M, Lu C-Z, Liu C-E, Liao S-C, Chen J-M, Guo Z and Pang WK (2018) Effect of AlF_3-Coated $Li_4Ti_5O_{12}$ on the Performance and Function of the $LiNi_{0.5}Mn_{1.5}O_4$||$Li_4Ti_5O_{12}$ Full Battery—An in-operando Neutron Powder Diffraction Study. Front. Energy Res. 6:89. doi: 10.3389/fenrg.2018.00089

The $LiNi_{0.5}Mn_{1.5}O_4$ ||$Li_4Ti_5O_{12}$ (LMNO||LTO) battery possesses a relatively-high energy density and cycle performance, with further enhancement possible by application of an AlF_3 coating on the LTO electrode particles. We measure the performance enhancement to the LMNO||LTO battery achieved by a AlF_3 coating on the LTO particles through electrochemical testing and use *in-operando* neutron powder diffraction to study the changes to the evolution of the bulk crystal structure during battery cycling. We find that the AlF_3 coating along with parasitic Al doping slightly increases capacity and greatly increases rate capability of the LTO electrode, as well as significantly reducing capacity loss on cycling, facilitating a gradual increase in capacity during the first 50 cycles. Neutron powder diffraction reveals a structural response of the LTO and LNMO electrodes consistent with a greater availability of lithium in the battery containing AlF_3-coated LTO. Further, the coating increases the rate of structural response of the LNMO electrode during charge, suggesting faster delithiation, and enhanced Li diffusion. This work demonstrates the importance of studying such battery performance effects within full configuration batteries.

Keywords: lithium ion battery, *in-operando*, neutron powder diffraction, real-time analysis, electrochemistry, protective coating, AlF_3

INTRODUCTION

Lithium ion batteries (LIBs) are the main choice of power source for portable electronic devices, including emerging electric vehicle (EV) and hybrid electric vehicle (HEV) technologies, as a result of their low cost, high energy/power density, and relatively long cycle life (Wang and Cao, 2008; Choi and Aurbach, 2016; Li et al., 2017a,b). The first commercial LIBs used lithium cobalt oxide ($LiCoO_2$) as the positive electrode and graphite as the negative electrode, however, the low energy density of this battery is insufficient to satisfy the demands of developing technology (Su et al., 2014; Li et al., 2017b), stimulating the exploration of novel electrode materials with higher energy/power capabilities than the existing state-of-the-art.

The performance limitation in existing LIB technology is the positive electrode, with new materials possessing both higher capacity and average working voltage required to further improve battery energy densities (Fergus, 2010; Liu et al., 2016). In recent years, layered positive electrode materials related to $LiCoO_2$, such as $LiNi_{1/3}Mn_{1/3}Co_{1/3}O_2$ (NMC) and $LiNi_{0.8}Co_{0.15}Al_{0.05}O_2$ (NCA), have been extensively studied and are now used commercially as a result of their relatively-high capacity (Li et al., 2018). However, these materials possess a relatively-low working potential (∼3.7 V vs. Li/Li^+) and suffer from severe voltage decay, limiting their application (Gu et al., 2012; Zheng et al., 2013). Other positive electrode materials with high voltage such as $LiMn_2O_4$ (4.0 V vs. Li/Li^+) (Kim et al., 2008; Xia et al., 2016), $LiNi_{0.5}Mn_{1.5}O_4$ (LNMO) (∼4.7 V vs. Li/Li^+) (Liu et al., 2016; Ma et al., 2016; Pang et al., 2016), and $LiCoAsO_4$ (4.6 V vs. Li/Li^+) (Arroyo-de Dompablo and Amador, 2006; Satya Kishore and Varadaraju, 2006), have also been studied with the aim of improving LIB performance. The LNMO material is arguably the most promising positive electrode material for the next-generation of high-energy-density LIBs, due to its high working voltage, low fabrication cost, relative environmental friendliness, and reasonable cycle stability (Liu et al., 2016; Pang et al., 2016). Moreover, LNMO possesses a practical capacity of more than 140 mAh g^{-1} and an average working voltage of 4.7 V (vs. Li/Li^+), resulting in an exceptionally high energy density, reaching as high as 650 Wh kg^{-1}, beyond that of most other LIB positive electrode materials such as $LiFePO_4$ at ∼560 Wh kg^{-1}, $LiMn_2O_4$ at ∼480 Wh kg^{-1}, and $LiMn_{1/3}Ni_{1/3}Co_{1/3}O_2$ at ∼510 Wh kg^{-1} (Croy et al., 2014; Pang et al., 2016).

LNMO crystalizes into a cubic structure which can have two different atom arrangements, one being a phase with $P4_332$ space group and the other having $Fd\bar{3}m$ space group symmetry (Ariyoshi et al., 2004; Kim et al., 2004; Santhanam and Rambabu, 2010; Feng et al., 2011; Pang et al., 2014b). Both these phases exhibit similar electrochemical performance, with the $Fd\bar{3}m$ phase being slightly more favorable due to faster Li ion diffusion and high structural stability (Feng et al., 2011), where the $P4_332$ space group phase suffers multiple cubic/cubic two-phase reactions during cycling, resulting in phase segregation and grain boundary movement, limiting the Li diffusion rate.

Positive electrode materials such as LNMO are commonly paired with a carbonaceous negative electrode in a full LIB, but this negative electrode suffers from lithium dendrite growth, especially at high rate, and the formation of a thick solid electrolyte interphase (SEI) at voltage <0.8 V vs. Li/Li^+, further deteriorating rate performance and cycle life (Wang et al., 2001; Zhang, 2006). Another negative electrode commonly paired with LNMO is the so-called "zero-strain" $Li_4Ti_5O_{12}$ (LTO) material, with a plateau at 1.55 V vs. Li/Li^+ and superb structural stability and stable cycle performance (Pang et al., 2014b). Although the working voltage of a LIB containing LTO is reduced a little relative to the carbonaceous negative electrode, the issues associated with lithium dendrite and SEI formation can be effectively avoided, enabling superior cycle life.

Consequently, full LIBs containing LTO counter electrodes have been intensively studied, with the $LiMn_2O_4||Li_4Ti_5O_{12}$ full-cell noted to have good safety and electrochemical performance (Belharouak et al., 2007; Wang et al., 2014). However, a major drawback of the $LiMn_2O_4||Li_4Ti_5O_{12}$ system is its relatively low working voltage of ∼2.5 V, limiting its high-energy application. Alternative LNMO||LTO systems with higher working voltages have been investigated, aiming for a working voltage of ∼3.2 V (Ariyoshi and Ohzuku, 2007; Xiang et al., 2008; Wu et al., 2009; Li et al., 2013; Zhang et al., 2013). Ariyoshi and Ohzuku (2007) first reported a 3 V LNMO||LTO system, expected to be widely used in lead-free accumulators, EVs, and HEVs. A further barrier to achieving high voltage LNMO||LTO is the stability of organic-carbonate-based electrolytes, and Xiang et al. enhanced the operational safety of this electrode combination by using a non-flammable dimethyl methylphosphonate (DMMP) based electrolyte (Xiang et al., 2007).

Nevertheless, even with these advancements, the performance of the LNMO||LTO system remains limited by the cycle life of the spinel positive electrode, where the material undergoes two-phase behavior at higher voltages, and suffers from Jahn-Teller distortion resulting in the dissolution of Mn into the electrolyte (Xiao et al., 2013). To resolve these issues, electrode modifications have been adopted, such as doping LNMO with the aim of avoiding Jahn-Teller distortion and coating the active material particle surface to minimize attack of the hydrofluoric acid produced during electrolyte decomposition (Deng et al., 2014; Kim et al., 2014, 2015). Compared with doping strategies, surface coating is more popular due to its simplicity and high efficiency. AlF_3 is commonly used as protecting layer on electrode particles, avoiding the direct exposure to the electrolyte (Wu et al., 2015) and effectively mitigating against the hydrofluoric acid produced by electrolyte decomposition at high voltage (Zheng et al., 2014; Sun et al., 2015; Zhou et al., 2017), as well as against severe gassing behavior of LTO known to occur during cycling (Li et al., 2014). LNMO and $Li[Li_{0.2}Ni_{0.17}Co_{0.07}Mn_{0.56}]O_2$ coated with AlF_3 exhibit better electrochemical performance (Sun et al., 2015; Wu et al., 2015). However, the majority of research into the effect of AlF_3 coatings on electrode particles focus on the positive electrode, and work studying the modified LTO material in a full-configuration battery is lacking.

In this work, we performed a comparative study to investigate how an AlF_3 coated LTO enhances the electrochemical performance of a LNMO||LTO full-configuration battery using high-resolution and *in-operando* neutron powder diffraction (NPD). NPD has been widely employed to perform mechanistic studies of active electrode materials in LIBs. The nuclear scattering mechanism sometimes results in elemental contrast that is difficult to achieve using X-ray diffraction, such as a high sensitivity to lighter elements (i.e., Li and O) in the presence of heavier elements and to transition metals with a similar number of electrons. For example, the elements in a LNMO||LTO battery, Li, Ni, Mn, O, and Ti, have coherent neutron scattering lengths of −1.9, 10.3, −3.7, 5.8, and −3.4 fm, respectively, making NPD one of the most powerful analytical tools for this study (Pang et al., 2014b, 2017; Zhao et al., 2017). Further, the high penetration depth and non-destructive nature of neutrons, as well as advanced modern detectors and instrumentation, enable the real-time monitoring of structural changes of active electrode materials inside functioning LIBs

(Pang et al., 2014a,b, 2016, 2017). Using NPD, the Li content and location within the LNMO and LTO electrodes can be measured, yielding information that is crucially important to understand the functional mechanism of the LNMO||LTO battery. For example, Zhao et al. (2017) explored the relationship between the Li^+/Ni^{2+} ion exchange rate and electrochemical performance of the $LiNi_xMn_yCo_{1-x-y}O_2$ positive electrode, and our previous work (Pang et al., 2014b, 2017) revealed the structural evolution in detail of LNMO and Li diffusion path within the LTO electrode in a LNMO||LTO full battery using *in-operando* NPD. We note the capability of NPD to examine in detail 18650-standard full-configuration batteries, making the approach of industrial relevance in the analysis of the real-time phase transformation and structural change inside commercial batteries.

Our present NPD study of the AlF_3 coated LTO within a LNMO||LTO full-configuration battery reveals that the AlF_3 coated LTO enhances cycle stability of the battery as well as inducing faster structural response of the LNMO counter electrode during its solid solution behavior during charge.

EXPERIMENTAL DETAILS

LNMO powders were prepared by a co-precipitation method. $NiSO_4{\cdot}6H_2O$ (98%, Sigma Aldrich) and $MnSO_4{\cdot}H_2O$ (98%, Sigma Aldrich) (1:3 mole ratio) were added into distilled water and stirred to obtain a homogenous aqueous solution. The solution was pumped into a reactor at 50°C and the pH was kept at 10.5 by adding NH_4OH aqueous solution (28%, Sigma Aldrich) to obtain the homogenous $Ni_{0.25}Mn_{0.75}(OH)_2$ precursors. These precursors were then thoroughly mixed with lithium carbonate (Li_2CO_3) powders (99%, Sigma Aldrich) and calcined at 750°C for 12 h to obtain LNMO powders.

To synthesize LTO, a sol-gel method was used. Lithium acetate (98%, Sigma Aldrich) and tetrabutyltitanate (98%, Sigma Aldrich) (4:5 mole ratio) were mixed with citric acid (99%, Sigma Aldrich) in ethanol (99.5%, Sigma Aldrich). A homogenous white gel was formed after aging the mixed solution for 3 h. The white gel was then heated at 80°C to obtain an organic precursor and the precursor was further calcined at 800°C for 3 h to yield fine LTO powders.

To prepare AlF_3-modified LTO, ammonium fluoride (99%, Aldrich) and aluminum nitrate nonahydrate (99%, Aldrich) were dissolved in distilled water. LTO powders were immersed into the aluminum nitrate solution and the ammonium fluoride solution was slowly added to achieve a ratio of Al:F of 1:3 where the amount of AlF_3 in the solution corresponded to 10 wt% of LTO. The solution containing the LTO powders was constantly stirred at 80°C for 5 h and then filtered using distilled water. Subsequently, the obtained LTO powders were heated at 400°C for 3 h under flowing nitrogen to avoid the formation of Al_2O_3.

The morphology of LNMO, LTO, and AlF_3-coated LTO were investigated by scanning electron microscopy (SEM) using a JEOL JSM7500 and transmission electron microscopy (TEM) using a 200 kV JEOL 2011. Elemental mapping using energy dispersive spectroscopy (EDS) was performed using a JEOL ARM-200F aberration-corrected transmission electron microscope. The phase and composition of the LNMO, LTO, and AlF_3-coated LTO were also characterized using a combination of laboratory XRPD carried out on a Shimadzu Corporation 6000 X-ray diffractometer equipped with a Cu source and high-resolution NPD performed on the high-resolution neutron powder diffractometer ECHIDNA (Liss et al., 2006) at the Open Pool Australian Light water (OPAL) research reactor at the Australian Nuclear Science and Technology Organization (ANSTO). High-resolution NPD data were collected over the 2θ angular range 4–164° with a step size of 0.125° with neutrons of wavelength 1.6218(3) Å as determined using the $La^{11}B_6$ National Institute of Standards and Technology (NIST) standard reference material 660b. Structural analysis was performed using a joint refinement against both XRPD and NPD data using the GSAS-II software (Toby and Von Dreele, 2013). Refined parameters included the background coefficients, zero offset, peak shape parameters. Refined phase parameters included the lattice parameter, oxygen positional parameter, isotropic atomic displacement parameters, and site occupancy factors.

Positive electrodes were prepared by mixing LNMO, polyvinylidene difluoride (PVDF), and carbon black (super P) in a weight ratio of 83:7:10 with N-methyl-2-pyrrolidinone (NMP). After continuously stirring for 3 h the homogenous slurry was coated onto aluminum foil and dried in vacuum at 120°C for 12 h. Negative electrodes were prepared by mixing LTO, PVDF, and super P in a weight ratio of 80:10:10 in NMP, which was stirred, and then coated onto copper foil, and then dried using that same procedure as for the positive electrode preparation.

The electrochemical performance of the LNMO, LTO, and AlF_3-LTO as working electrodes in half-configuration coin cells was tested. Half cells were assembled using Li foil as counter electrode and Celgard® 2400 polypropylene membrane as separator. The electrolyte used was 1M $LiPF_6$ in ethylene carbonate (EC) and dimethyl carbonate (DMC) in a 1:1 ratio by volume. The cell was assembled in an Ar-filled glove box ($O_2 < 1$ ppm, $H_2O < 1$ ppm) and prepared cells galvanostatically tested using a LAND multichannel battery testing system (CT2001A).

18650-standard full-configuration 900–1000 mAh batteries were assembled at the Industrial Technology Research Institute (ITRI) in Taiwan. The performance of the LNMO||LTO systems were evaluated in these batteries between 0.5 and 3.3 V (vs. LTO) using a Maccor series 4000 (USA). These 18650-standard full-configuration batteries were also used in *in-operando* NPD experiments with WOMBAT (Studer et al., 2006), the high-intensity neutron powder diffractometer at ANSTO (a schematic is shown in **Figure S1**). Data were collected every minute over a 2θ angular range 20-136.9° using neutrons of 2.4123(2) Å, as determined using the $La^{11}B_6$ NIST standard reference material 660b, during cycling within 2.0–3.4 V at a current of 0.09 A (equivalent to ∼0.1 C). Single-peak fitting of LTO and LNMO reflections was performed using the Large Array Manipulation Program (Richard et al., 1996).

RESULTS AND DISCUSSION

The morphology and particle size of LTO and AlF_3-coated LTO as characterized using SEM and TEM are shown in **Figures 1a,c**

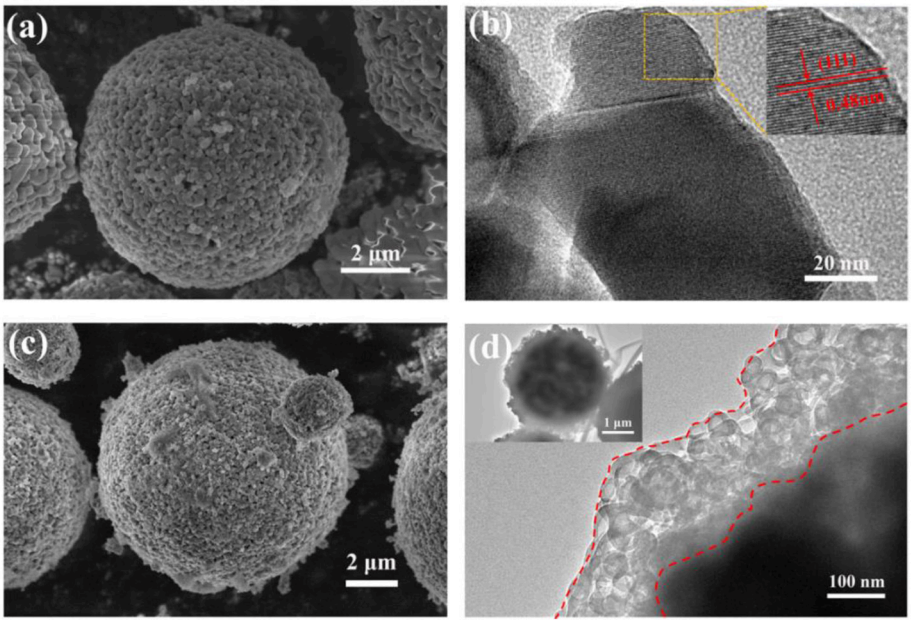

FIGURE 1 | SEM micrographs of **(a)** LTO and **(c)** AlF_3-coated LTO; TEM micrographs of **(b)** LTO with inset showing a magnification of the area outlined in yellow with fringes across the (111), and **(d)** AlF_3-coated LTO with inset showing a whole particle at lower magnification.

and **Figures S2a,b**, revealing that the secondary particles of both LTO and AlF_3-coated LTO are highly porous microspheres with a diameter of 3–10 μm and composed of primary particles of ∼50 nm in diameter. These morphology features promote electrolyte permeation. **Figure 1b** reveals crystalline pristine LTO where the observed (111) lattice (inset) has a spacing of approximately ∼0.48 nm, as consistent with the LTO structure (Cao et al., 2015; Wang et al., 2015). **Figure 1d** shows a uniform coating on the LTO particle, of thickness 100∼200 nm. Results of elemental mapping using EDS are shown in **Figure S3**, clearly revealing a uniform distribution of Al and F around a particle with a central core of Ti and O, confirming a uniform AlF_3 coating. The morphology of the LNMO material is shown in **Figures S2c,d**, where LNMO microspheres are 3-12 μm in diameter and composed of bar-like primary particles ∼500 nm in diameter and ∼2 μm in length.

Structural refinement results for LTO and AlF_3 coated LTO, as well as LNMO materials performed using both high-resolution NPD and XRPD data are shown in **Table 1** and **Table S1**, respectively, and the corresponding Rietveld refinement profiles in **Figure 2** and **Figure S3**, respectively. The LTO and AlF_3 coated LTO phase are both found to be cubic with a $Fd\bar{3}m$ space group (Pang et al., 2014b). The lattice parameter of the LTO is slightly smaller in the coated material, possibly as a result of the doping of ∼3% Al into the LTO structure, as found in the crystallographic analysis and in good agreement with previous work reporting the partial substitution of Al at the 16*c* site in the LTO spinel (Xu et al., 2013; Li et al., 2014). We identify the parasitic doping of Al into the LTO structure in our crystallographic analysis, which was not performed in previous studies of AlF_3-coated electrodes (Sun et al., 2007; Tron et al., 2016), despite Al doping in LTO being associated with improved cycling stability and better rate capability (Xu et al., 2013). We note the possibility of the doping of F onto the O site, however, the determination of this is very difficult given the low contrast for these elements in both NPD and XRPD data, as noted in a previous study (Pang et al., 2017).

Our analysis also revealed that both LTO samples contain minor phases of Li_2O (space group $Fm\bar{3}m$, Inorganic Crystal Structure Database entry number 54368), Li_2O_2 (space group $P6_3/mmc$, Inorganic Crystal Structure Database entry number 50658) and rutile-type TiO_2 (space group $P4_2/mnm$, Inorganic Crystal Structure Database entry number 31324) in the phase composition reported in **Table 2**. We note a larger fraction of rutile in the AlF_3-coated LTO, further supporting the doping of Al in the LTO. Although these minor phases result in a slight reduction in capacity, we focus on the LTO behavior in the following discussion.

The inherently lower resolution of the NPD data relative to the XRPD data meant that the AlF_3 was only detectable in the XRPD data. The Rietveld refinement profile using XRPD data of the AlF_3-coated LTO sample is shown in **Figure S4**, revealing weight fractions of LTO:AlF_3 to be 89(1):11(1) in good agreement with the nominal composition used in the synthesis.

The LNMO sample is found to be composed of both $P4_332$ and $Fd\bar{3}m$ space group phases of amounts 22(2) and 78(2)%, respectively (**Table S1** and **Figure S5**). The lattice and atomic parameters of both phases of LNMO are summarized in **Table S1**. The charge-discharge curve of half cells containing LNMO appear similar to that of those for cells containing only the $Fd\bar{3}m$ space group LNMO phase (**Figure S6**), confirming that the

TABLE 1 | Crystallographic details of LTO and AlF_3-coated LTO obtained from joint Rietveld analysis using XRPD and NPD data. U_{iso} is the isotropic atomic displacement parameter.

$Li_4Ti_5O_{12}$ Space Group = *Fd* $\bar{3}$ *m* *a* = 8.3505(2)Å, Volume = 582.30(4) Å^3						
Atom	**Site**	***x***	***y***	***z***	**U_{iso} (Å^2)**	**Site occupancy factor**
Li	8*a*	0.375	0.375	0.375	0.015(1)	1
Li	16*d*	0	0	0	0.0100(3)[a]	0.167
Ti	16*d*	0	0	0	0.0100(3)[a]	0.833
O	32*e*	0.23754(4)[b]	0.23754(4)[b]	0.23754(4)[b]	0.0087(2)	1
AlF_3-coated $Li_4Ti_5O_{12}$ Space Group = *Fd*$\bar{3}$*m*						
a = 8.3447(2)Å, Volume = 581.07(5) Å^3						
Atom	**site**	***x***	***y***	***z***	**U_{iso} (Å^2)**	**Site occupancy factor**
Li	8*a*	0.375	0.375	0.375	0.025(1)	1
Li	16*d*	0	0	0	0.0106(4)[c]	0.167
Ti	16*d*	0	0	0	0.0106(4)[c]	0.802(3)[e]
Al	16*d*	0	0	0	0.0106(4)[c]	0.031(3)[e]
O	32*e*	0.23752(4)[d]	0.23752(4)[d]	0.23752(4)[d]	0.0121(2)	1

[a,b,c,d]constrained to be the same. [e]constrained to sum to 0.833.

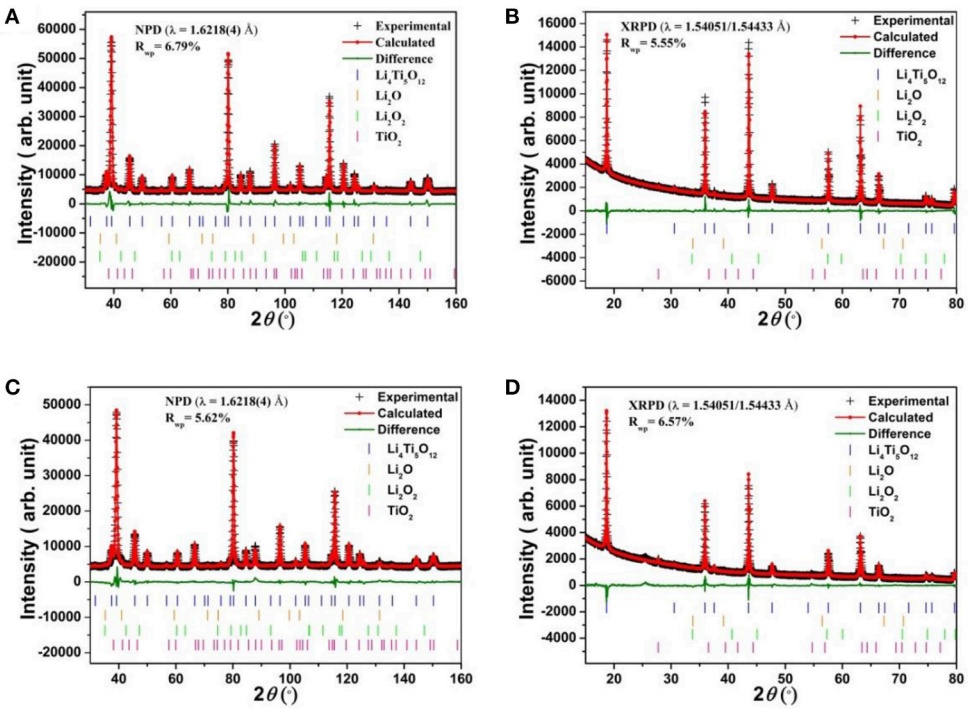

FIGURE 2 | Rietveld refinement profiles for **(A)** NPD and **(B)** XRPD data of LTO, and **(C)** NPD and **(D)** XRPD data of AlF_3-coated LTO. The combined goodness-of-fit (GOF) are 2.58 and 2.15, respectively, and R_{wp} is the weighted profile R-factor.

majority of the sample is composed of LNMO with *Fd*$\bar{3}$*m* space group, which is considered in the following discussion.

The electrochemical performance of the pristine LTO and AlF_3-coated LTO in half-cells are shown in **Figure 3**. **Figure 3A** shows the cycling performance of both LTO at a current density of 1 C (1 C = 175 mA g^{-1}). The uncoated LTO delivers a similar but slightly higher capacity performance (discharge capacity of 162 mAh g^{-1} and charge capacity of 149 mAh g^{-1}) than the

TABLE 2 | Phase composition of LTO and AlF_3-coated LTO samples (AlF_3 excluded).

	Weight fraction (%)			
	LTO	Li_2O	Li_2O_2	TiO_2 (rutile)
LTO	94.66(5)	4.0(1)	0.44(4)	0.9(1)
AlF_3-coated LTO	93.10(5)	3.6(2)	0.40(4)	2.9(2)

AlF_3-coated LTO, which has a capacity of 157 mAh g^{-1} and a charge capacity of 142 mAh g^{-1}. The slightly lower charge capacity of the coated LTO is attributed to the addition of the AlF_3 [11(1) wt.%], which makes no contribution to lithium storage. When the LTO component only is considered, the charge capacity of AlF_3-coated LTO is 159 mAh g^{-1}, ∼85 and 91% of the theoretical charge capacity in the uncoated and coated LTO, respectively.

In terms of cycling performance, the AlF_3-coated LTO retains ∼93% of capacity after 265 cycles compared with ∼81% by the uncoated LTO. The average capacity decay per cycle of LTO and AlF_3-coated LTO is ∼0.070 and ∼0.025%, respectively, with the nearly 300% improvement in the cycling stability of the coated sample attributed to protection against hydrofluoric acid attack. Whilst the underlying mechanism for the known issue of gassing of LTO is yet to fully understood, it is thought to originate from a reaction of Ti and electrolyte, initiating the electrolyte decomposition (Han et al., 2017), and the AlF_3-coating may also help to prevent this behavior. Further contributing to this enhanced cycling stability may be the parasitic Al doping induced by the coating, where the Al-O bond strengthens the MO_6 octahedron (Huang et al., 2007).

Figure 3B compares the rate capabilities of the uncoated and coated LTO. We note that our reported capacities are only for the LTO content of the electrode. The uncoated LTO delivers a capacity of 158, 154, and 146 mAh g^{-1} at a current density of 0.2 C, 0.5 C, and 1 C, respectively, lower than those of the AlF_3-coated LTO of 163, 158, and 156 mAh g^{-1} when the LTO component is considered only, respectively. However, at larger current densities of 2 C and 4 C, the AlF_3-coated LTO anode delivers a capacity of 153 and 147 mAh g^{-1} (considering only the LTO component), respectively, much higher than for the uncoated LTO (122 and 90 mAh g^{-1}, respectively). The improved rate capability of the AlF_3-coated LTO is ascribed to enhanced ionic conductivity as a result of both the coating and Al doping into the structure. We note that the capacity of both uncoated and coated LTO recovered to almost their original value in the first ten cycles at 0.2 C, of 157 and 143 (161 for only the LTO component) mAh g^{-1}, respectively.

Figures 3C,D show the 1st, 50th, and 200th charge-discharge curves of the uncoated and AlF_3-coated LTO at 1 C. In the 1st cycle, the typical plateaus of LTO (∼1.6 V during charge and ∼1.4 V during discharge) are observed for both samples. The AlF_3-coated LTO is found to have a lower degree of polarization (0.17 V) than the uncoated LTO (0.25 V). Upon cycling, the polarization of the uncoated LTO increases dramatically after 200 cycles, where the curve becomes distorted without recognizable plateaus. On the contrary, plateaus in 200th charge-discharge curve for AlF_3-coated LTO are observed at 1.58 V and 1.51 V during delithiation and lithiation process, respectively, indicating enhanced structural stability and cycling performance.

Full battery test results using 18650-type LNMO||LTO batteries are shown in **Figure S7**. At 0.1 C, the LNMO||AlF_3-coated LTO battery delivered a charge capacity of 1097 mAh and a discharge capacity of 944 mAh, constituting ∼86% coulombic efficiency in the first cycle (**Figure S7a**). The first-cycle irreversible capacity was 153 mAh and the overlapped discharge curves of the first and second cycle indicate a stable cycling performance. **Figure S7b** shows the rate performance of the full battery, where the rate-induced potential polarization only increases slightly with increasing current density and the curve retaining obvious plateaus during both charge and discharge. These results reveal superior reaction kinetics of the LNMO||AlF_3-coated LTO full battery relative to the battery containing uncoated LTO. A comparison of the electrochemical performance of the 18650-type full cells containing uncoated and coated LTO is shown in **Figures S7c,d**, respectively. The battery containing the coated LTO has a slightly lower capacity, commensurate with the reduced amount of active LTO, and greatly enhanced cycle performance. Further, unlike the uncoated LTO battery, a gradual increasing capacity during cycling at 1 C was observed in the battery with the coated LTO during the first 50 cycles (**Figures S7c,d**).

To elucidate the mechanism for the enhanced performance of the LNMO||LTO battery achieved by the AlF_3 coating of the LTO, we employed *in-operando* NPD to investigate the phase and structure evolution of the electrodes in 18650 batteries containing LNMO and either coated or uncoated LTO. Full-angular-range contour plots of *in-operando* NPD data in different cycles of the LNMO||LTO batteries and LNMO||AlF_3-coated LTO batteries are shown in **Figure S8**. To show the structural response of the electrodes in more detail, **Figure 4** shows contour plots of the NPD data for both batteries in a selected 2θ range. The 18650-type batteries contain conventional organic hydrogenated electrolyte and Celgard® 2400 separator, both of which are rich in hydrogen and lead to a significant background in the NPD data. Nevertheless, the evolution of the LTO 222 and LNMO 222 reflections during cycling are clearly observed. As LTO is a "zero strain" lithium insertion electrode, the LTO 222 reflection position change during battery cycling is expected to be small. Despite this, the minor lattice change (peak shift) can be clearly observed. We employ single peak fitting of this LTO 222 reflection to understand further the structural evolution of the LTO phase, with the results shown in **Figures 5**, **6** for the LNMO||LTO and LNMO||AlF_3-coated LTO batteries, respectively.

The positional shift of the LTO 222 reflection during the 1st and 2nd cycle is shown in **Figure 5A**, and for the 51st cycle in **Figure 5B**. The positional shift is similar for the first and second cycle, where during lithiation, the LTO 222 reflection shifts to lower 2θ, then to the higher 2θ, indicating the LTO lattice first expands and then contracts. As the end of lithiation is approached, the LTO 222 reflection shows a minor shift to lower 2θ before its final maximum is reached at the charged

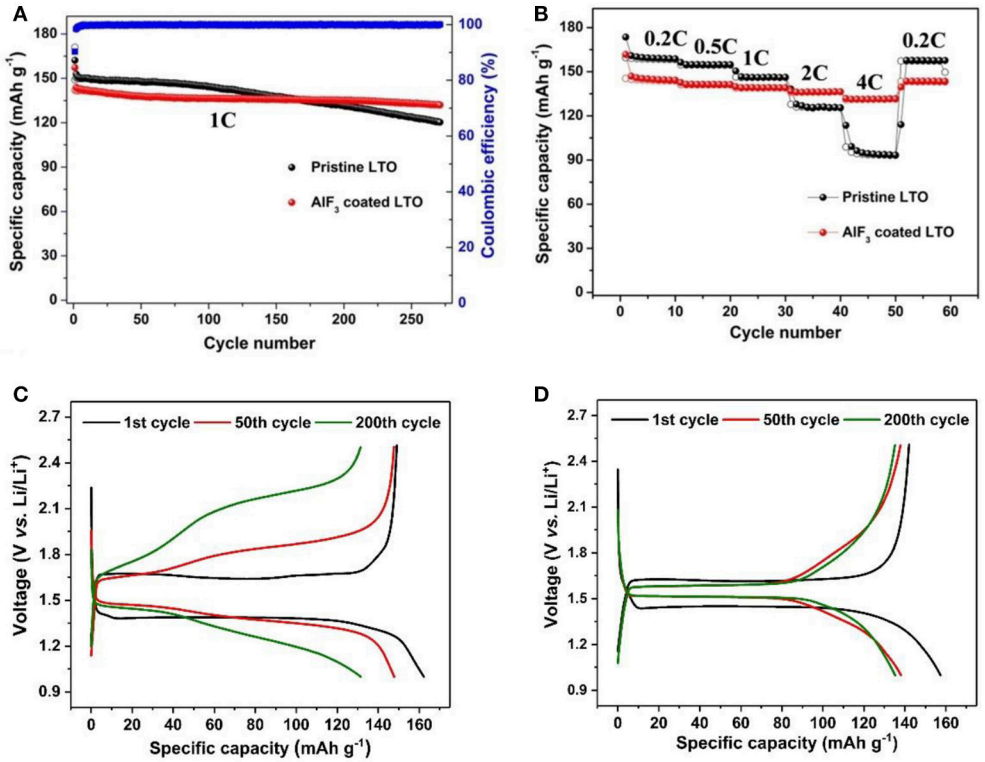

FIGURE 3 | (A) Cycling performance and coulombic efficiency of LTO and AlF_3-coated LTO at 1 C up to 260 cycles; **(B)** rate performance of LTO and AlF_3-coated LTO; 1st, 50th, and 200th charge-discharge curves of **(C)** LTO and **(D)** AlF_3-coated LTO at 1 C. The capacity of AlF_3-coated LTO sample is measured for the composite, including electrochemically active LTO and inactive AlF_3.

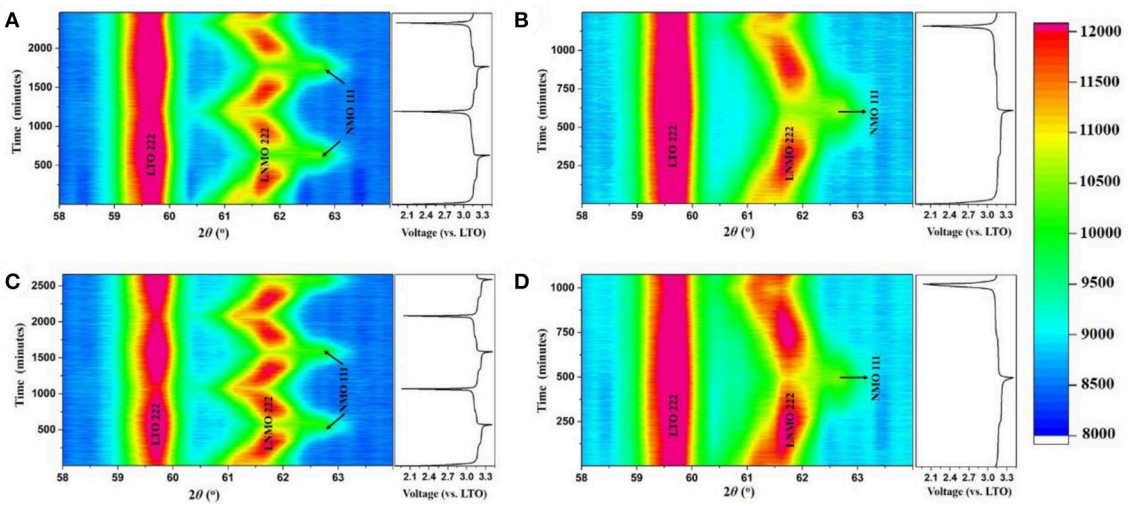

FIGURE 4 | Contour plot of *in-operando* NPD data of the LNMO||LTO battery **(A)** for the first two cycles and **(B)** for the 51st cycle, and of the LNMO||AlF_3-coated LTO battery **(C)** for the first two cycles and **(D)** for the 51st cycle, with intensity (arb.) shown in color with the scale and corresponding voltage curve on the right. LTO 222 and LNMO 222 as well as NMO 111 reflections are labeled.

state. This response is completely consistent with that previously reported, where during lithiation lithium is transferred from the 8*a*, through 32*e*, to the 16*c* crystallographic sites, and the change in structure captured by the LTO 222 reflection position corresponds to the changing population of lithium at these sites, in addition to the repositioning of the O atom in response to lithiation of the 16*c* site (Pang et al., 2014a,b). In the 51st cycle the behavior of the LTO 222 reflection is reproduced, except the

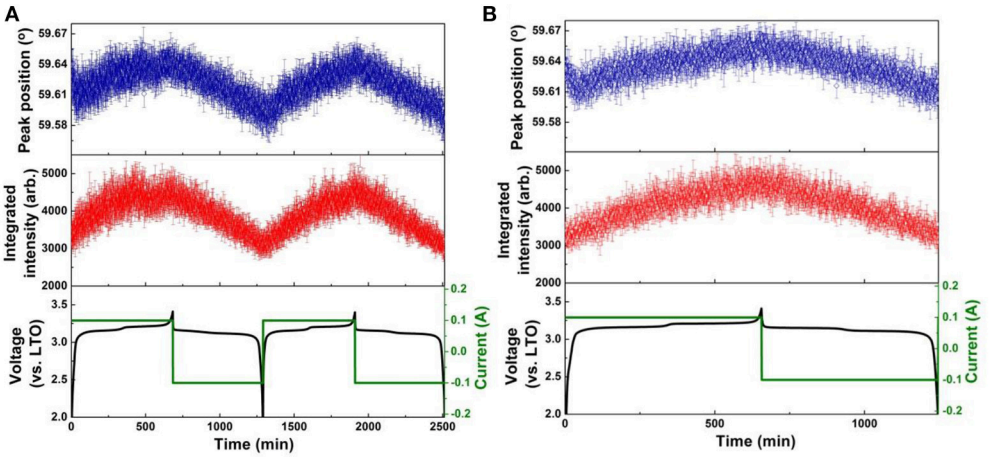

FIGURE 5 | Results of single peak fitting of the LTO 222 reflection in NPD data of the LNMO||LTO battery, including peak position and intensity for **(A)** the first two cycles, and **(B)** the 51st cycle. Battery voltage and current are shown alongside.

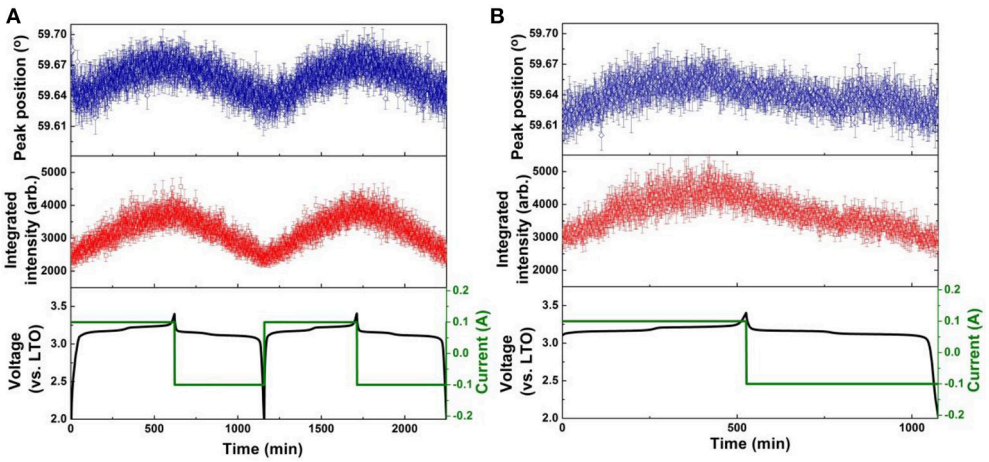

FIGURE 6 | Results of single peak fitting of the LTO 222 reflection in NPD data of the LNMO||AlF_3-LTO battery, including peak position and intensity for **(A)** the first two cycles, and **(B)** the 51st cycle. Battery voltage and current are shown alongside.

transitions are less marked, suggesting some decay of electrode function. Delithiation during discharge induces a relatively linear shift in the LTO 222 reflection position to lower 2θ (expansion), as consistent again with previous work and the known behavior of the LTO electrode (Pang et al., 2014a,b).

The positional shift of the AlF_3-coated LTO 222 reflection in the first and second cycles (**Figure 6A**) shows a similar trend to that of the uncoated LTO, except the minor shift to lower 2θ (expansion) prior to the end of lithiation is only barely observable. The position shift of the AlF_3-coated LTO 222 reflection reaches a maximum plateau before the end of lithiation, implying that the capacity of LTO in this battery has not been fully delivered (Pang et al., 2014b). In the 51st cycle (**Figure 6B**), the minor shift to lower 2θ just prior to the fully charged battery state observed clearly in the 1st and 2nd charge for the uncoated LTO, is just beginning to appear for the coated LTO. In contrast to the uncoated LTO, the position shift of the AlF_3-coated LTO 222 reflection during delithiation exhibits two partially discernible stages for the 1st and 2nd discharge, with this behavior becoming more pronounced in the 51st discharge (**Figure 6B**). The maximum difference in lattice parameter during the 1st, 2nd, and 51st cycle for the coated and uncoated LTO was calculated from the positional shift of the LTO 222 reflection and is shown **Table 3**. These results clearly show that the AlF_3 coating alongside the parasitic doping of Al that occurs reduces the overall LTO lattice change during battery cycling.

The integrated intensity of the LTO 222 reflection is closely associated with the amount of lithium residing at 8*a* and 16*c*, as well as the 32e, crystallographic sites, as well as the position of the oxygen responding to the changing lithium concentration at these sites (Pang et al., 2014a). The intensity of this reflection for both coated and uncoated samples increases during lithiation. The anomalous shift in the LTO 222 reflection position just prior

to the maximum lithiated state is mimicked by the reflection intensity, where a decrease followed by an increase just prior to its maximum is observed. As consistent with the differences in the trend of the LTO 222 reflection position between the uncoated and coated LTO, the intensity change just prior to maximum lithiation is also more pronounced in the uncoated LTO, being hardly visible for the coated LTO. The evolution of the LTO 222 reflection intensity also becomes less pronounced at the 51st cycle, particularly for the uncoated LTO. Similar to the evolution of the LTO 222 reflection position during delithiation, the intensity evolution is more monotonic for the uncoated sample and somewhat staged for the coated LTO in the 51st cycle.

We note that in the AlF_3-coated LTO it may be possible for Al^{3+} to migrate from the 16*d* site occupied by the Ti to the 16*c* site normally occupied by Li^+, resulting in different oxygen repositioning known to occur for the undoped (uncoated) LTO. Such effects may contribute to differences in both the LTO 222 reflection position and intensity evolution. The coherent neutron-scattering length of Al is +3.4 fm, while that of Li is −1.9 fm. Hence, the migration of Al to the 16*c* site is expected to reduce reflection intensity, consistent with a premature finish of the lithiation, although it is difficult to disentangle this effect from that of the O repositioning. A premature completion of lithiation due to Al migration may also explain the gradual increasing capacity observed for the coated LTO-containing battery during cycling at 1 C in the first 50 cycles (**Figures S7c,d**), where an activation process enabling full capacity (∼175 mAh g^{-1}) is correlated with the slight shift to lower 2θ (expansion) near the end of lithiation (just observable in the 51st cycle for the coated LTO).

The evolution of LNMO counter electrode structure in the LNMO||LTO and LNMO||AlF_3-coated LTO batteries is also examined using single peak fitting of the LNMO 222 reflection with results shown in **Figures 7**, **8**. Our previous work (Pang et al., 2014b) revealed that $Fd\bar{3}m$ LNMO undergoes a solid-solution reaction during the redox Ni^{2+}/Ni^{3+} reaction between 3.06 and 3.16 V vs. LTO with a lattice change associated with lithium extraction and insertion. In the present work, we quantify the rate of lithium extraction from the LNMO during the initial charge process by the rate of change of the peak position (° per min) extracted from linear fitting of the time evolution of the LNMO 222 reflection position (**Figures S9, S10**), with the result given in **Table 3**. The LNMO delithiation rate in the LNMO||LTO battery remains nearly unchanged for 50 cycles, but increases gradually in the AlF_3-coated LTO battery. This result implies that the AlF_3 coating promotes faster lithium transport between the electrodes, possibly via a protection by the AlF_3 of the LTO against both hydrofluoric acid and deposition of Mn known to be released by the LNMO, a cause of capacity fade in graphite counter electrodes (Tsunekawa et al., 2002), and allowing the LNMO to continue lithiation/delithation unhindered on continued cycling. We also note that the LNMO||AlF_3-LTO battery, unlike the LNMO||LTO battery, exhibits a capacity increase during cycling (see **Figures S7c,d**), which indicates an increased availability of lithium to shuttle between the electrodes. **Table 3** shows the maximal change

TABLE 3 | Comparison of maximum change of the coated and uncoated LTO lattice parameter, as well as the corresponding rate of change and maximum position change in the counter electrode LNMO 222 reflection position during the charging solid-solution-reaction stage when cycling.

	1st cycle	2nd cycle	51st cycle
Maximum lattice parameter change of LTO and AlF_3-coated LTO (%)			
Uncoated LTO	0.044(1)	0.042(1)	0.040(1)
AlF_3-coated LTO	0.040(1)	0.037(1)	0.035(1)
Rate of change of LNMO 222 reflection position (°per min)			
LNMO||LTO	0.001330(9)	0.001340(9)	0.001300(7)
LNMO||AlF_3-coated LTO	0.001200(7)	0.001370(9)	0.001440(1)
Maximum change of LNMO 222 reflection position (%)			
LNMO||LTO	0.0045(1)	0.0040(1)	0.0033(2)
LNMO||AlF_3-coated LTO	0.0015(2)	0.0016(2)	0.0032(2)

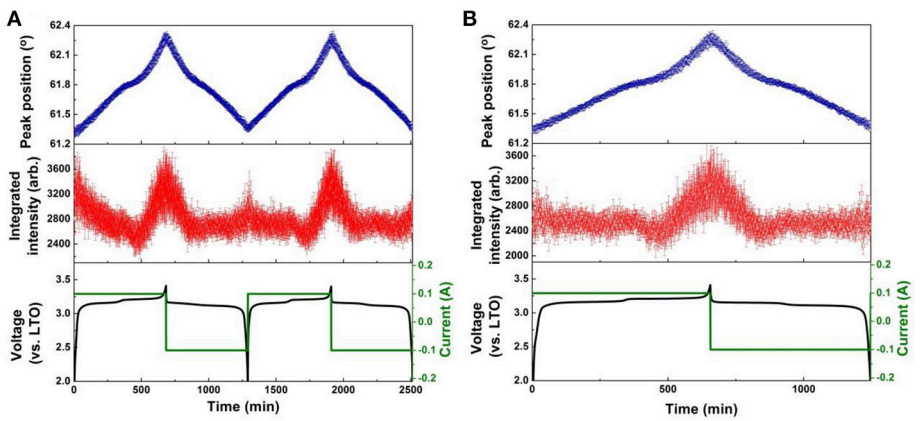

FIGURE 7 | Results of single peak fitting of the LNMO 222 reflection of NPD data for the LNMO||LTO battery, including peak position and intensity, for **(A)** the first two cycles, and **(B)** the 51st cycle. Battery voltage and current are also shown.

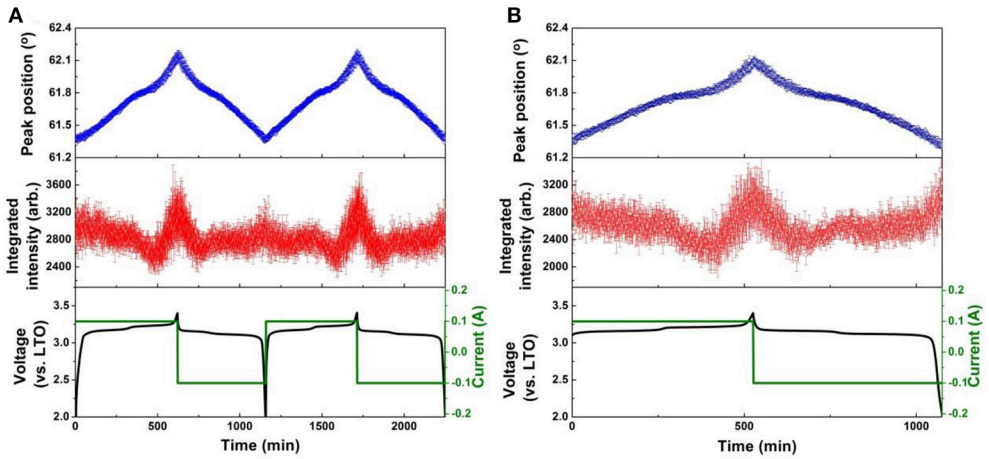

FIGURE 8 | Results of single peak fitting of the LNMO 222 reflection of NPD data for the LNMO||AlF_3-LTO battery, including peak position and intensity, for **(A)** the first two cycles, and **(B)** the 51st cycle. Battery voltage and current are also shown.

of the LNMO 222 reflection position at different cycles in the battery containing the coated and uncoated LTO. The maximum positional change of the LNMO 222 reflection in the LNMO||LTO battery decreases on cycling, while that in the LNMO||AlF_3-LTO battery increases during cycling, consistent with a higher reservoir of active lithium in the battery containing the coated LTO. Further, this result is also corroborated by the structural response of the LTO lattice parameter, where the co-distribution of Li at 8*a* and 16*c* crystallographic sites results in a lattice expansion followed by contraction during lithiation, and therefore a lower maximal lattice change at higher degree of lithiation (Pang et al., 2014a), evidencing higher lithiation in both electrodes in the battery containing the coated LTO.

CONCLUSIONS

The effect of an AlF_3 coating on LTO within a LTO||LNMO battery on the performance and structural evolution of electrodes was investigated by a combination of electrochemical testing and *in-operando* neutron powder diffraction. The coating is found to cause the doping of approximately 3% Al onto the 16*c* crystallographic site of the disordered LTO phase structure. Our examination of the structural response of LTO and LNMO during battery cycling reveals that the AlF_3 coating alongside the induced parasitic doping of Al enhances capacity of the LTO, and suppresses capacity decay in the battery. We measure changes to the structural response of the LTO and LNMO electrodes within the battery containing the coated LTO that are consistent with a greater availability of lithium, and an enhanced rate of lithium extraction from the LNMO counter electrode during its solid-solution behavior on charge. This work demonstrates the feasibility of an LNMO||AlF_3-coated LTO full battery, and our study of the effect of the AlF_3 coating within the full battery configuration reveals new insights into the mechanism of battery performance enhancement.

AUTHOR CONTRIBUTIONS

K-YK prepared the AlF_3 coated LTO. C-MC prepared the 18650 batteries. GL and AP performed preliminary characterization of samples as well as prepared and tested coin cells. C-ZL, C-EL, J-MC, and S-CL performed full battery performance characterization. GL, VP, and WP collected and analyzed the neutron data and prepared the manuscript. WP, VP, and ZG directed the research.

ACKNOWLEDGMENTS

The authors acknowledge the financial support funded from the Ministry of Economic Affairs (MOEA) of TAIWAN, the Australia Neutron Science and Technology Organization (ANSTO) for neutron beamtime, and the Australian Research Council for FT150100109, FT160100251, and DP170102406. In addition, the authors would like to thank the Australian Institute of Nuclear Science and Engineering (AINSE) Limited for providing financial assistance in the form of a Post Graduate Research Award (PGRA) to enable this work. The authors would also be grateful to the Electron Microscopy Centre (EMC) at the University of Wollongong for the support and equipment assistance.

SUPPLEMENTARY MATERIAL

The Supplementary Material for this article can be found online at: https://www.frontiersin.org/articles/10.3389/fenrg.2018.00089/full#supplementary-material

REFERENCES

Ariyoshi, K., Iwakoshi, Y., Nakayama, N., and Ohzuku, T. (2004). Topotactic two-phase reactions of $Li[Ni_{1/2}Mn_{3/2}]O_4$ ($P4_332$) in nonaqueous lithium cells. *J. Electrochem. Soc.* 151, A296–A303. doi: 10.1149/1.1639162

Ariyoshi, K., and Ohzuku, T. (2007). Conceptual design for 12V "lead-free" accumulators for automobile and stationary applications. *J. Power Sources* 174, 1258–1262. doi: 10.1016/j.jpowsour.2007.06.085

Arroyo-de Dompablo, M. E., and Amador, U. (2006). A computational investigation on the electrochemical properties of spinel-like $LiCoAsO_4$ as positive electrode for lithium-ion batteries. *Solid State Sci.* 8, 916–921. doi: 10.1016/j.solidstatesciences.2006.02.051

Belharouak, I., Sun, Y. K., Lu, W., and Amine, K. (2007). On the safety of the $Li_4Ti_5O_{12}$/ $LiMn_2O_4$ lithium-ion battery system. *J. Electrochem. Soc.* 154, A1083–A1087. doi: 10.1149/1.2783770

Cao, L., Hui, Y., Ouyang, H., Huang, J., Xu, Z., Li, J., et al. (2015). $Li_4Ti_5O_{12}$ hollow mesoporous microspheres assembled from nanoparticles for high rate lithium-ion battery anodes. *RSC Adv.* 5, 35643–35650. doi: 10.1039/C5RA03158C

Choi, J. W., and Aurbach, D. (2016). Promise and reality of post-lithium-ion batteries with high energy densities. *Nat. Rev. Mater.* 1:16013. doi: 10.1038/natrevmats.2016.13

Croy, J. R., Abouimrane, A., and Zhang, Z. (2014). Next-generation lithium-ion batteries: the promise of near-term advancements. *MRS Bull.* 39, 407–415. doi: 10.1557/mrs.2014.84

Deng, H., Nie, P., Luo, H., Zhang, Y., Wang, J., and Zhang, X. (2014). Highly enhanced lithium storage capability of $LiNi_{0.5}Mn_{1.5}O_4$ by coating with Li_2TiO_3 for Li-ion batteries. *J. Mater. Chem. A* 2, 18256–18262. doi: 10.1039/C4TA03802A

Feng, X., Shen, C., Fang, X., and Chen, C. (2011). Synthesis of $LiNi_{0.5}Mn_{1.5}O_4$ by solid-state reaction with improved electrochemical performance. *J. Alloys Compounds* 509, 3623–3626. doi: 10.1016/j.jallcom.2010.12.116

Fergus, J. W. (2010). Recent developments in cathode materials for lithium ion batteries. *J. Power Sources* 195, 939–954. doi: 10.1016/j.jpowsour.2009.08.089

Gu, M., Belharouak, I., Zheng, J., Wu, H., Xiao, J., Genc, A., et al. (2012). Formation of the spinel phase in the layered composite cathode used in Li-ion batteries. *ACS Nano* 7, 760–767. doi: 10.1021/nn305065u

Han, C., He, Y. B., Liu, M., Li, B., Yang, Q. H., Wong, C. P., et al. (2017). A review of gassing behavior in $Li_4Ti_5O_{12}$-based lithium ion batteries. *J. Mater. Chem. A* 5, 6368–6381 doi: 10.1039/C7TA00303J

Huang, S., Wen, Z., Zhu, X., and Lin, Z. (2007). Effects of dopant on the electrochemical performance of $Li_4Ti_5O_{12}$ as electrode material for lithium ion batteries. *J. Power Sources* 165, 408–412. doi: 10.1016/j.jpowsour.2006.12.010

Kim, D. K., Muralidharan, P., Lee, H. W., Ruffo, R., Yang, Y., Chan, C. K., et al. (2008). Spinel $LiMn_2O_4$ nanorods as lithium ion battery cathodes. *Nano Lett.* 8, 3948–3952. doi: 10.1021/nl8024328

Kim, J. H., Myung, S. T., Yoon, C. S., Kang, S. G., and Sun, Y. K. (2004). Comparative study of LiNi0.5Mn1.5O4-δ and LiNi0.5Mn1.5O4 cathodes having two crystallographic structures: $Fd\bar{3}m$ and $P4_332$ *Chem. Mater.* 16, 906–914. doi: 10.1021/cm035050s

Kim, J. H., Pieczonka, N. P. W., Sun, Y. K., and Powell, B. R. (2014). Improved lithium-ion battery performance of $LiNi_{0.5}Mn_{1.5-x}Ti_xO_4$ high voltage spinel in full-cells paired with graphite and $Li_4Ti_5O_{12}$ negative electrodes. *J. Power Sources* 262, 62–71. doi: 10.1016/j.jpowsour.2014.03.107

Kim, J. W., Kim, D. H., Oh, D. Y., Lee, H., Kim, J. H., Lee, J. H., et al. (2015). Surface chemistry of $LiNi_{0.5}Mn_{1.5}O_4$ particles coated by Al_2O_3 using atomic layer deposition for lithium-ion batteries. *J. Power Sources* 274, 1254–1262. doi: 10.1016/j.jpowsour.2014.10.207

Li, S., Chen, C., Xia, X., and Dahn, J. (2013). The impact of electrolyte oxidation products in $LiNi_{0.5}Mn_{1.5}O_4/Li_4Ti_5O_{12}$ cells. *J. Electrochem. Soc.* 160, A1524–A1528. doi: 10.1149/2.051309jes

Li, W., Dolocan, A., Oh, P., Celio, H., Park, S., Cho, J., et al. (2017a). Dynamic behaviour of interphases and its implication on high-energy-density cathode materials in lithium-ion batteries. *Nat. Commun.* 8:14589. doi: 10.1038/ncomms14589

Li, W., Li, X., Chen, M., Xie, Z., Zhang, J., Dong, S., et al. (2014). AlF_3 modification to suppress the gas generation of $Li_4Ti_5O_{12}$ anode battery. *Electrochim. Acta* 139, 104–110. doi: 10.1016/j.electacta.2014.07.017

Li, W., Liu, X., Celio, H., Smith, P., Dolocan, A., Chi, M., et al. (2018). Mn versus Al in layered oxide cathodes in lithium-ion batteries: a comprehensive evaluation on long-term cyclability. *Adv. Energy Mater.* 8:1703154. doi: 10.1002/aenm.201703154

Li, W., Song, B., and Manthiram, A. (2017b). High-voltage positive electrode materials for lithium-ion batteries. *Chem. Soc. Rev.* 46, 3006–3059. doi: 10.1039/C6CS00875E

Liss, K. D., Hunter, B., Hagen, M., Noakes, T., and Kennedy, S. (2006). Echidna–the new high-resolution powder diffractometer being built at OPAL. *Phys. B: Condensed Matter* 385–386, 1010–1012. doi: 10.1016/j.physb.2006.05.322

Liu, H., Wang, J., Zhang, X., Zhou, D., Qi, X., Qiu, B., et al. (2016). Morphological evolution of high-voltage spinel $LiNi_{0.5}Mn_{1.5}O_4$ cathode materials for lithium-ion batteries: the critical effects of surface orientations and particle size. *ACS Appl. Mater. Interfaces* 8, 4661–4675. doi: 10.1021/acsami.5b11389

Ma, J., Hu, P., Cui, G., and Chen, L. (2016). Surface and interface issues in spinel $LiNi_{0.5}Mn_{1.5}O_4$: insights into a potential cathode material for high energy density lithium ion batteries. *Chem. Mater.* 28, 3578–3606. doi: 10.1021/acs.chemmater.6b00948

Pang, W. K., Lin, H. F., Peterson, V. K., Lu, C. Z., Liu, C. E., Liao, S. C., et al. (2017). Effects of fluorine and chromium doping on the performance of lithium-rich $Li_{1+x}MO_2$ (M= Ni, Mn, Co) positive electrodes. *Chem. Mater.* 29, 10299–10311. doi: 10.1021/acs.chemmater.7b02930

Pang, W. K., Lu, C. Z., Liu, C. E., Peterson, V. K., Lin, H. F., Liao, S. C., et al. (2016). Crystallographic origin of cycle decay of the high-voltage $LiNi_{0.5}Mn_{1.5}O_4$ spinel lithium-ion battery electrode. *Phys. Chem. Chem. Phys.* 18, 17183–17189. doi: 10.1039/C6CP00947F

Pang, W. K., Peterson, V. K., Sharma, N., Shiu, J. J., and Wu, S. H. (2014a). Lithium migration in $Li_4Ti_5O_{12}$ studied using in situ neutron powder diffraction. *Chem. Mater.* 26, 2318–2326. doi: 10.1021/cm5002779

Pang, W. K., Sharma, N., Peterson, V. K., Shiu, J. J., and Wu, S. H. (2014b). In-situ neutron diffraction study of the simultaneous structural evolution of a $LiNi_{0.5}Mn_{1.5}O_4$ cathode and a $Li_4Ti_5O_{12}$ anode in a $LiNi_{0.5}Mn_{1.5}O_4||Li_4Ti_5O_{12}$ full cell. *J. Power Sources* 246, 464–472. doi: 10.1016/j.jpowsour.2013.07.114

Richard, D., Ferrand, M., and Kearley, G. (1996). Analysis and visualisation of neutron-scattering data. *J. Neutron Res.* 4, 33–39. doi: 10.1080/10238169608200065

Santhanam, R., and Rambabu, B. (2010). Research progress in high voltage spinel $LiNi_{0.5}Mn_{1.5}O_4$ material. *J. Power Sources* 195, 5442–5451. doi: 10.1016/j.jpowsour.2010.03.067

Satya Kishore, M. V. V. M., and Varadaraju, U. V. (2006). Synthesis, characterization and electrochemical studies on $LiCoAsO_4$. *Mater. Res. Bull.* 41, 601–607. doi: 10.1016/j.materresbull.2005.09.005

Studer, A. J., Hagen, M. E., and Noakes, T. J. (2006). Wombat: the high-intensity powder diffractometer at the OPAL reactor. *Phys. B: Condensed Matter* 385–386, 1013–1015. doi: 10.1016/j.physb.2006.05.323

Su, X., Wu, Q., Li, J., Xiao, X., Lott, A., Lu, W., et al. (2014). Silicon-based nanomaterials for lithium-ion batteries: a review. *Adv. Energy Mater.* 4:1300882. doi: 10.1002/aenm.201300882

Sun, S., Yin, Y., Wan, N., Wu, Q., Zhang, X., Pan, D., et al. (2015). AlF_3 surface-coated $Li[Li_{0.2}Ni_{0.17}Co_{0.07}Mn_{0.56}]O_2$ nanoparticles with superior electrochemical performance for lithium-ion batteries. *ChemSusChem* 8, 2544–2550. doi: 10.1002/cssc.201500143

Sun, Y. K., Cho, S. W., Lee, S. W., Yoon, C., and Amine, K. (2007). AlF_3-coating to improve high voltage cycling performance of $Li[Ni_{1/3}Co_{1/3}Mn_{1/3}]O_2$ cathode materials for lithium secondary batteries. *J. Electrochem. Soc.* 154, A168–A172. doi: 10.1149/1.2422890

Toby, B. H., and Von Dreele, R. B. (2013). GSAS-II: the genesis of a modern open-source all purpose crystallography software package. *J. Appl. Crystallogr.* 46, 544–549. doi: 10.1107/S0021889813003531

Tron, A., Park, Y. D., and Mun, J. (2016). AlF_3-coated $LiMn_2O_4$ as cathode material for aqueous rechargeable lithium battery with improved cycling stability. *J. Power Sources* 325, 360–364. doi: 10.1016/j.jpowsour.2016.06.049

Tsunekawa, H., Tanimoto, S., Marubayashi, R., Fujita, M., Kifune, K., and Sano, M. (2002). Capacity fading of graphite electrodes due to the deposition of manganese ions on them in Li-ion batteries. *J. Electrochem. Soc.* 149, A1326–A1331. doi: 10.1149/1.1502686

Wang, C., Appleby, A. J., and Little, F. E. (2001). Electrochemical impedance study of initial lithium ion intercalation into graphite powders. *Electrochim. Acta* 46, 1793–1813. doi: 10.1016/S0013-4686(00)00782-9

Wang, C., Wang, S., He, Y. B., Tang, L., Han, C., Yang, C., et al. (2015). Combining fast li-ion battery cycling with large volumetric energy density: grain boundary induced high electronic and ionic conductivity in $Li_4Ti_5O_{12}$ spheres of densely packed nanocrystallites. *Chem. Mater.* 27, 5647–5656. doi: 10.1021/acs.chemmater.5b02027

Wang, Y., and Cao, G. (2008). Developments in nanostructured cathode materials for high-performance lithium-ion batteries. *Adv. Mater.* 20, 2251–2269. doi: 10.1002/adma.200702242

Wang, Z., Wang, Z., Peng, W., Guo, H., and Li, X. (2014). An improved solid-state reaction to synthesize Zr-doped $Li_4Ti_5O_{12}$ anode material and its application in $LiMn_2O_4$/$Li_4Ti_5O_{12}$ full-cell. *Ceramics Int.* 40, 10053–10059. doi: 10.1016/j.ceramint.2014.04.011

Wu, H., Belharouak, I., Deng, H., Abouimrane, A., Sun, Y. K., and Amine, K. (2009). Development of $LiNi_{0.5}Mn_{1.5}O_4$/$Li_4Ti_5O_{12}$ system with long cycle life. *J. Electrochem. Soc.* 156, A1047–A1050. doi: 10.1149/1.3240197

Wu, Q., Yin, Y., Sun, S., Zhang, X., Wan, N., and Bai, Y. (2015). Novel AlF_3 surface modified spinel $LiMn_{1.5}Ni_{0.5}O_4$ for lithium-ion batteries: performance characterization and mechanism exploration. *Electrochim. Acta* 158, 73–80. doi: 10.1016/j.electacta.2015.01.145

Xia, H., Xia, Q., Lin, B., Zhu, J., Seo, J. K., and Meng, Y. S. (2016). Self-standing porous $LiMn_2O_4$ nanowall arrays as promising cathodes for advanced 3D microbatteries and flexible lithium-ion batteries. *Nano Energy* 22, 475–482. doi: 10.1016/j.nanoen.2016.01.022

Xiang, H. F., Jin, Q. Y., Chen, C. H., Ge, X. W., Guo, S., and Sun, J. H. (2007). Dimethyl methylphosphonate-based nonflammable electrolyte and high safety lithium-ion batteries. *J. Power Sources* 174, 335–341. doi: 10.1016/j.jpowsour.2007.09.025

Xiang, H. F., Zhang, X., Jin, Q. Y., Zhang, C. P., Chen, C. H., and Ge, X. W. (2008). Effect of capacity matchup in the $LiNi_{0.5}Mn_{1.5}O_4$/$Li_4Ti_5O_{12}$ cells. *J. Power Sources* 183, 355–360. doi: 10.1016/j.jpowsour.2008.04.091

Xiao, X., Ahn, D., Liu, Z., Kim, J. H., and Lu, P. (2013). Atomic layer coating to mitigate capacity fading associated with manganese dissolution in lithium ion batteries. *Electrochem. Commun.* 32, 31–34. doi: 10.1016/j.elecom.2013.03.030

Xu, W., Chen, X., Wang, W., Choi, D., Ding, F., Zheng, J., et al. (2013). Simply AlF_3-treated $Li_4Ti_5O_{12}$ composite anode materials for stable and ultrahigh power lithium-ion batteries. *J. Power Sources* 236, 169–174. doi: 10.1016/j.jpowsour.2013.02.055

Zhang, S. S. (2006). The effect of the charging protocol on the cycle life of a Li-ion battery. *J. Power Sources* 161, 1385–1391. doi: 10.1016/j.jpowsour.2006.06.040

Zhang, Z., Hu, L., Wu, H., Weng, W., Koh, M., Redfern, P. C., et al. (2013). Fluorinated electrolytes for 5 V lithium-ion battery chemistry. *Energy Environ. Sci.* 6, 1806–1810. doi: 10.1039/c3ee24414h

Zhao, E., Fang, L., Chen, M., Chen, D., Huang, Q., Hu, Z., et al. (2017). New insight into Li/Ni disorder in layered cathode materials for lithium ion batteries: a joint study of neutron diffraction, electrochemical kinetic analysis and first-principles calculations. *J. Mater. Chem. A* 5, 1679–1686. doi: 10.1039/C6TA08448F

Zheng, J., Gu, M., Xiao, J., Polzin, B. J., Yan, P., Chen, X., et al. (2014). Functioning mechanism of AlF_3 coating on the Li-and Mn-rich cathode materials. *Chem. Mater.* 26, 6320–6327. doi: 10.1021/cm502071h

Zheng, J., Gu, M., Xiao, J., Zuo, P., Wang, C., and Zhang, J. G. (2013). Corrosion/fragmentation of layered composite cathode and related capacity/voltage fading during cycling process. *Nano Lett.* 13, 3824–3830. doi: 10.1021/nl401849t

Zhou, Y., Lee, Y., Sun, H., Wallas, J. M., George, S. M., and Xie, M. (2017). Coating solution for high-voltage cathode: AlF_3 atomic layer deposition for freestanding $LiCoO_2$ electrodes with high energy density and excellent flexibility. *ACS Appl. Mater. Interfaces* 9, 9614–9619. doi: 10.1021/acsami.6b15628

Conflict of Interest Statement: The authors declare that the research was conducted in the absence of any commercial or financial relationships that could be construed as a potential conflict of interest.